PCCP

Accepted Manuscript

ROYAL SOCIETY OF CHEMISTRY

www.rsc.org/pccp

Journal Name

ARTICLE

Structural and functional insights into the conductive pili of *Geobacter sulfurreducens* revealed in molecular dynamics simulations

Received 00th January 20xx,
Accepted 00th January 20xx

DOI: 10.1039/x0xx00000x

www.rsc.org/

G. T. Feliciano,[a] R. J. Steidl[b] and G. Reguera[b*]

Geobacter sulfurreducens (GS) electronically connects with extracellular electron acceptors using conductive protein filaments or pili. To gain insights into their role as biological nanowires, we investigated the structural dynamics of the GS pilus in solution via molecular dynamics simulations. In the model, all of the pilin's aromatics clustered as a right-handed helical band along the pilus, maintaining inter-aromatic distances and dimer configurations optimal for multistep hopping. The aromatics were interspersed within the regions of highest negative potential, which influenced the type and configuration of the aromatic contacts and the rates of electron transfer. Small foci of positive potential were also present but were neutralized within uncharged regions, thus minimizing charge trapping. Consistent with the model predictions, mutant strains with reduced aromatic contacts or negative potentials had defects in pili functions such as the reduction of Fe(III) oxides and electrodes. The results therefore support the notion of a pilus fiber evolved to function as an electronic conduit between the cell and extracellular electron acceptors.

Introduction

Geobacter bacteria gain energy for growth from the extracellular reduction of Fe(III) oxides and metal contaminants such as uranium, which are processes that require the expression of conductive pili. [1, 2] The pili are also required for the formation of electrochemically active biofilms and maximum current production in bioelectrochemical cells.[4, 5] As in other bacteria with type IV pili,[7] the pili of *Geobacter* are an assembly of a peptide subunit or pilin that carries the conserved N-terminal sequence of type IVa pilins.[1, 2] Yet conservation does not extend to the C-t region, which is divergent in structure and amino acid composition in a manner that is consistent with a peptide environment optimized for electron conduction.[8] The pilin of the model representative *Geobacter sulfurreducens* (GS) lacks, for example, the conserved C-terminal globular head of type IVa pilins,[8] which contains the αβ-loop and anti-parallel β-sheet domains of bacterial pilins that confer on the pili their distinctive shape, surface chemistry, and biological functions such as adhesion, surface motility and cell-cell aggregation.[9] In the GS pilin, the globular head is replaced by a short, flexible C-t random-coiled segment.[8] As a result, most of the pilin's amino acids reside in the conserved α-helix region (α1 domain),[8] a structural conformation that promotes electronic coupling and charge transport.[10] Furthermore, amino acid conservation in the helical region is restricted to the N-terminal portion (α1-N domain).[8] Not surprisingly, the *Geobacter* pilins form an independent line of descent among bacterial pilins.[1]

Though the conductance of the GS pilus fiber has been demonstrated with various approaches,[1, 11, 12] the mechanism underlying its conductivity remains controversial. A metallic model was proposed to explain the metallic-like temperature-dependence of piliated, electrochemically active biofilms and crude preparations of pili and other proteins, including cytochromes, dried on gold electrodes.[13] The metallic conductance model relies heavily on the assumption that phenyl and phenol rings in phenylalanine and tyrosine residues, respectively, are stacked in π-π configurations in the pilus fiber.[13] However, structural information about the GS pilus is lacking and insights into inter-aromatic distances and the configuration aromatic contacts are limited to predictions from homology models.[3, 14, 15] Bonanni *et al.* [14] superimposed a GS pilin computational homology model onto each of the subunits of the high-resolution structural model of the *Neisseria gonorrhoeae* (gonococal or GC) pilus, which was constructed from crystallographic and cryo-EM data.[6] The modeled pilus fiber revealed the periodic and helical arrangement of aromatic residues within distances (15-21 Å) optimal for charge hopping but too large to allow for π orbital stacking. The same template was used to construct another homology model using the solution NMR structure of the GS pilin.[3] In this model, the aromatic residues clustered within a radius of 15 Å and were interspersed within aromatic-free

[a] Departamento de Físico-Química, Instituto de Quimica, Universidade Estadual Paulista Júlio de Mesquita Filho (UNESP), Nanobionics group, Araraquara, Sao Paulo, Brazil
[b] Department of Microbiology and Molecular Genetics, Michigan State University, East Lansing MI 48824, USA.
* Email: reguera@msu.edu
† Electronic Supplementary Information (ESI) available: PDB files of all the structural models. See DOI: 10.1039/x0xx00000x

regions, raising questions about how charges can be transported from one aromatic-rich region to the next. Using a similar model Yan *et al.* [16] calculated inter-aromatic distances (6.5 to 10.8 Å) too large (and theoretical charge transport properties too low) to support metallic conductance based on aromatic contacts. By contrast, a homology model constructed using a *Pseudomonas aeruginosa* strain K (PAK) computational pilus model as a template,[17] revealed the uniform clustering of aromatic residues within distances (3 to 4 Å) that could promote π orbital stacking and metallic conductance.[15]

The accuracy of homology models of protein assemblies depends greatly on the structural conservation of the interacting subunits.[18] But even for closely related proteins, intermolecular interactions can differ significantly.[19] Hence, discrepancies in the predictions inferred from the GS pilus homology models may reflect differences in the structural assumptions used to construct each model. One way to improve the accuracy of a homology model is to refine it to higher resolution in molecular dynamics (MD) simulations.[20] Hence, we used experimentally validated structures of the GS pilin [3] and a type IV pilus template (the gonococcal or GC pilus)[6] to construct a high resolution structural model of the GS pili in solution via MD simulations. We also tested the model predictions experimentally in biological assays that evaluated the ability of pili carrying targeted amino acid replacements to reduce Fe(III) oxide minerals or to wire electrochemically active biofilms. Taken together, the theoretical and experimental results support the notion of a peptide assembly optimized for multistep hopping and provide critical insights into the role that aromatics and their electrostatic environment play in charge transport.

Materials and Methods

Homology modeling of the GS pilus

A homology model of a GS pilus fiber was first constructed using the NMR-derived GS pilin structure [3] and the *Neisseria gonorrhoeae* or gonococcus (GC) pilus fiber resolved by cryo-electron microscopy (PDB: 2HIL) [6] as a template. MD simulations with the software suite GROMACS [21-23] were first used to relax each of the 18 GS pilin structures obtained from the last frame of the NMR analyses (PDB: 2M7G). This first MD step refined the pilin structural model in explicit water so as to improve geometry and structural statistics (distance restraint violations < 0.5 Å and dihedral angle violations < 5°). The MD relaxation of the GS pilin consisted of a 20 ns run. The structure with the lowest root-mean-square deviation (RMSD = 2.78 Å with respect to the backbone), which is provided in the supplemental pilin-WT.pdb file, was aligned with each of the subunits of the cryo-EM GC pilus. The regions of highest homology (the α-helix portion or α1 domain, residues 2-50) between the GS and GC pilins were superimposed and the fit between the N-t helices was optimized (RMSD = 2.91 Å) using the SWISSMODEL workspace operated in automatic modeling mode.[24, 25] This approach generated a GS homology model (supplemental homoGPIL-WT.pdb file), which we used for the MD simulations described below.

Molecular Dynamics (MD) simulations of the GS pilus and mutated variants

All of the MD simulations were performed with the GROMACS software suite.[21-23] The homology model of the GS pilus was inserted in a 9 x 9 x 18 nm rectangular box and the system was subjected to a geometry optimization procedure using the AMBER99SB force field.[26] The steepest descent algorithm until the maximum force was smaller than 1000 kJ.nm^{-1}. At this moment, the cell was gradually shrunk until a periodic structure of the fiber was obtained after successive geometry optimizations. The optimized GS pilus was then solvated in water using the empirical TIP3P force field for pure liquid water [27] and the protonation states of the residues were set to match those at a pH of 7. Na and Cl ions (0.1 M) were then dissolved in the water to neutralize the net charge of the fiber per unit cell at this pH (-36 *e*, in the case of the wild-type [WT] GS pilus).

The number of water molecules used was such that the overall pressure of the system remained, in average, close to the room pressure for the original box (with the shortest distance among periodic images of the pili being □25 Å). The total number of atoms in the cell was ~130,000, with 16,956 atoms contributed by the GS pilin peptides. A first ns of MD was run with the empirical molecular mechanical (MM) potential for the protein with a fixed structure to allow the water and solute ions to relax around it, at 300 K, using the linear constraint solver algorithm (LINCS).[28] A second 1 ns run was used to fully relax the structure, but using an isobaric-isothermal (NPT) ensemble with a thermostat (T = 300 K) and a barostat (P = 1 bar) to allow for the pressure relaxation of the wet system. After equilibration, the MD simulation was run in production phase for 70 ns to obtain the MD trajectory of the GS pilus for analyses (supplemental GPIL-WT.pdb).

When indicated, mutations were introduced into the geometry-optimized GS pilus fiber to generate structural models of the Asp2 and Tyr3 mutant pili, which carry alanine replacements in two aspartic residues (D53A D54A) or the three tyrosines (Y27A Y32A Y57A) of the mature pilin peptide, respectively. The atomic coordinates for the Asp2 and Tyr3 GS pilus fibers are provided in supplemental GPIL-Asp2.pdb and GPIL-Tyr3.pdb files, respectively. MD simulations for the mutant fibers were as described for the wild-type (WT) GS pilus except that the MD run was shorter (1 ns) and Na and Cl ions (0.1 M) were dissolved in the water to neutralize the net charge of the fibers per unit cell at this pH (-36 *e* for Tyr3 and 0 *e* for the Asp2).

Calculation of aromatic density and contacts, and electrostatic maps

The MD simulations were analyzed with the VMD program [29] to construct surface maps of aromatic density and electrostatic potential in the WT and mutant (Asp2 and Tyr3) GS pilus fibers. For the calculation of aromatic density, we averaged the

atomic positions of the aromatic residues over the 70 ns MD trajectories and plotted the resulting distribution in surface maps of the WT, Asp2, and Tyr3 pilus fibers, which show the probability distribution of all the atoms of the aromatic residues in the entire space. The electrostatic potential maps of the WT and mutant pilus fibers were also constructed using the VMD program by evaluating the Coulomb potential at the surface of the protein using the classical atom-centered charges from OPLS (Optimized Potentials for Liquid Simulations) force field.[30]

We also calculated the number of aromatic contacts in the modeled WT, Asp2, and Tyr3 pilus fibers. For these analyses, we used the routine g_select program of the GROMACS package.[31] Two aromatic residues were regarded as a contact whenever they had at least one pair of atoms at a distance of 5 Å or less. This does not necessarily imply π-π stacking, as the other carbon-carbon distances may be significantly different.

Bacterial strains and culture conditions

The strains used in this study were the wild-type (WT) strain of *Geobacter sulfurreducens* PCA,[32] a derivative (WT_{SPEC}) carrying the wild-type copy of the pilin *pilA* gene and a spectinomycin cassette, and the pilin mutant strains Asp2 and Tyr3, constructed as described below. The strains were routinely cultured anaerobically at 30°C in NB medium [33] or freshwater FW medium [2] supplemented with 15 mM acetate as the electron donor and 40 mM fumarate or 50 mM Fe(III) citrate as the electron acceptor, respectively. Cultures used as inoculum for the microbial electrolysis cells (MECs) were routinely grown in DB medium with 20 mM acetate and 40 mM fumarate, as previously described.[34]

Construction of recombinant strains

G. sulfurreducens PCA was used as genetic background to construct the recombinant strains Asp2 and Tyr3, which carry targeted chromosomal alanine replacements in the pilin *pilA* gene (GSU1496) and a spectimomycin resistance cassette (*aad*) downstream of the mutated *pilA* gene. The amino acid replacements in each mutant (designations are for the mature, processed GS pilin) were: D53A and D54A in Asp2 and Y27A, Y32A, and Y57A in Tyr3. As a control we also constructed a strain (WT_{SPEC}) in which the wild-type *pilA* allele fused to the spectinomycin cassette was reintroduced in the WT strain. All primers used to construct the recombinant strains are shown in Table 1. The general procedure was to PCR-amplify the wild-type *pilA* allele and its upstream chromosomal region with primers pilASpecF1 and R1 and to introduce targeted point mutations in *pilA* using the QuikChange Lightning Site-Directed Mutagenesis kit (Agilent Technologies) and primers listed in Table 1. The recombinant alleles were sequenced to confirm the mutation(s) before fusing them to a spectinomycin cassette (SPEC, amplified from plasmid pRG5 [35] with primer set SpecF and SpecR) and the downstream region of *pilA* (amplified with primers pilASpecF2 and R2). The three fragments were fused together by Overlap Extension PCR using the external forward and reverse primers. The DNA construct was then cloned in plasmid pCR®2.1-TOPO® TA vector (Invitrogen™), its sequence confirmed, and further amplified using the external primers. The linear fragment was purified on an agarose gel, and its sequence was confirmed again, before electroporating into electrocompetent cells of *G. sulfurreducens*. Selection of recombinant strains was performed on NBAF plates [33] supplemented with 75 µg/ml of spectinomycin.

TABLE 1. PCR primers used to generate amino acid replacement constructs.

Primer	PCR product	Sequence (5'-3')
pilASpec F1	pilA + upstream	GTGGTGAAGGGGTAGGTTGA
pilASpec R1	pilA + upstream	GTTAGGCGTCATCCTGTGCTTAACTT TCGGGCGGATAGG
pilASpec F2	pilA downstream	CAAGCCGACGCCGCTTCTTGATTAA ATACATACTGGAGG
pilASpec R2	pilA downstream	GCGACTTCCACTCGGTACC
SpecF	*aadA*	GCACAGGATGACGCCTAAC
SpecR	*aadA*	GAAGCGGCGTCGGCTTG
pilAY27A-1	pilAY27A+ upstream	TCCGCAGTTCTCGGCGGCTCGTGTC AAGGCGTAC
pilAY27A-2	pilAY27A+ upstream	GTACGCCTTGACACGAGCCGCCGA GAACTGCGGA
pilAY32A-1	pilAY32A+ upstream	GTATCGTGTCAAGGCGGCCAACAG CGCGGCGTC
pilAY32A-2	pilAY32A+ upstream	GACGCCGCGCTGTTGGCCGCCTTGA CACGATAC
pilAY57A-1	pilAY57A+ upstream	CCGCATTTGCTGATGATCAAACCGC TCCGCCCGAAAGTTAA
pilAY57A-2	pilAY57A+ upstream	TTAACTTTCGGGCGGAGCGGTTTGA TCATCAGCAAATGCGG
pilA-Asp2-1	pilAD53,54A+ upstream	GAGTCCGCATTTGCTGCTGCTCAAA CCTATCCGCCC
pilA-Asp2-2	pilAD53,54A+ upstream	GGGCGGATAGGTTTGAGCAGCAGC AAATGCGGACTC

Biological assays of pili function

The *in vivo* effect of the Asp2 and Tyr3 mutations was investigated by growing the recombinant strains in FW cultures supplemented with 15 mM acetate (FWA medium) and 100 mM poorly crystalline Fe(III) oxide. The strains were first grown in FWA medium with 50 mM Fe(III) citrate as the electron acceptor to late exponential phase (~35 mM of Fe(II), measured in HCl-acidified culture supernatant fluids with the ferrozine assay)[36]. The Fe(III) citrate cultures were then transferred (10% v/v) to FWA-Fe oxide cultures supplemented with 4 mM of the metal chelator nitriloacetic acid (NTA). NTA supplementation allowed strains with any pilus deficiency to grow with the Fe(III) oxides.[1] Late exponential phase cultures from the NTA-Fe oxide cultures (~ 35 mM of Fe(II) solubilized) were inoculated into triplicate FWA-Fe oxide cultures with or without 4 mM NTA supplementation. The amount of NTA carried over in the inoculum was approximately 0.4 (± 0.1) mM. The extent of Fe(III) oxide reduction was monitored periodically by measuring the amount of soluble Fe(II) in

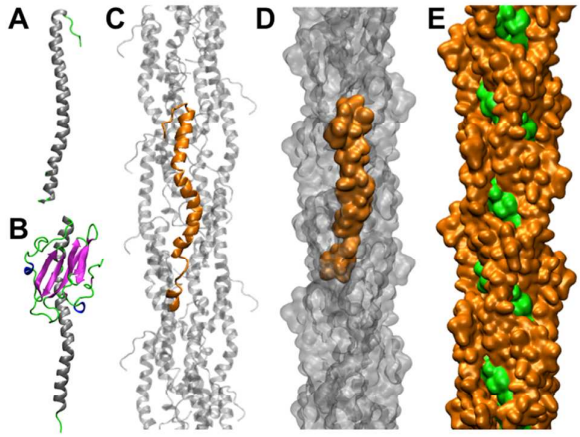

FIGURE 1. A-C. Snapshot of the favored GS pilin conformer (A) obtained from the MD simulation of the NMR structure resolved in micelles,[3] which was superimposed on the GC pilin structure (B) extracted from the cryo-EM structure of the GC pilus fiber [6] to construct a homology model of the GS pilus (C). D-E. Surface maps of the MD-optimized GS pilus highlighting, in orange, the position of one pilin (D) or showing the amino acids of the pilus fiber core (green) exposed to the solvent (E).

culture supernatant fluids acidified with 0.5 N HCl using the ferrozine method.[36]

The growth and electrochemical activity of the WT, Asp2, and Tyr3 strains was also assayed in H-type MECs equipped with three electrodes (anode and cathode graphite rod electrodes and a 3 M Ag/AgCl reference electrode). The MECs were set up, inoculated with cell suspensions of the corresponding strains, and operated with a poised anode electrode (0.24 V versus reference electrode) as described previously.[34] The electron donor in the anode chambers was acetate (1 mM). Supernatant samples were periodically removed from the anode chamber to monitor acetate consumption by high-performance liquid chromatography (HPLC), as described elsewhere.[37] Current production was recorded with a VSP potentiostat (BioLogic) and plotted against the time of MEC operation to assess the performance of the WT, Asp2, and Tyr3 anode biofilms, as described elsewhere.[34] At the end of the experiment, when all of the acetate had been oxidized and the current had dropped to basal levels, the anode electrodes were removed. The electrode-attached biofilms were stained with the BacLight™ viability kit (Invitrogen) and imaged with a FluoView FV1000 inverted microscope system (Olympus, Center Valley, PA) equipped with an Olympus UPLFLN 40X oil immersion objective (numerical aperture, 1.30), as described before.[34] Vertical 2D-images of the biofilms were collected every 1 µm from several random fields (1,024 by 1,024 pixels, 0.31 µm/pixel) per electrode, using a minimum of three biological MEC replicates, to calculate the biofilm thickness.

Results

Molecular dynamics (MD) simulations of the GS pilus

We used the atomic resolution NMR structure of the GS pilin [3] to build a homology model of the GS pilus using as a template the gonococcal GC pilus structure resolved with a combination of crystallography and cryo-EM.[6] As the NMR-derived pilin structure was derived from pilin monomers immersed in lipid micelles, we first refined its structure in solution in MD simulations (Figure 1A). The MD-optimized GS pilin was then docked onto each of the 18 pilin subunits (Figure 1B) of the GC pilus structural model to generate a homology model of the GS pilus fiber (Figure 1C).

The structure and dynamics of the solvated GS pilus was then investigated computationally in MD simulations. A snapshot extracted from the MD simulations is shown in Figure 1D. The favored conformer in solution was an ensemble in which the C-terminal (C-t) random coiled segment of individual pilin subunits was at a 40° angle with respect to the pilus fiber core, where the pilins' α-helices interact tightly. The average diameter of the pilus fiber core was 35 Å, but 47 Å when accounting for the volume occupied by the C-t random coil. Such diameters are within the ranges reported for the height of individual GS pilus fibers by atomic force microscopy [1] and scanning tunneling microscopy,[11] respectively. The tight intermolecular contacts between the α1 domains of neighboring pilins stabilized the structure of the pilus in the MD simulations. However, conformational rearrangements were observed in which the C-t contacts of the α1 domains (the α1-C domain) weakened, allowing for small gaps to form in the fiber's core that exposed otherwise buried amino acids to the solvent (Figure 1E). This is consistent with the structural plasticity reported for other type IV pili, which is critical for pilus function.[38, 39]

Once equilibrated, the structure of the GS pilin assembly revealed important intermolecular contacts (Figure 2). The model showed, for example, the alignment of the N-t phenylalanine (F1) of one subunit with the aspartic residue E5 of a neighboring subunit (Figure 2A). Such electrostatic interactions are required for *in vivo* pilin assembly [9] and determine the conserved 10.5 Å axial rise between

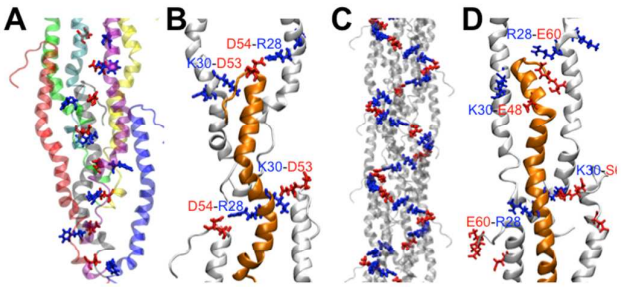

FIGURE 2. A. Intermolecular contacts between F1 (blue) and E5 (red) of neighboring pilins. B. Salt bridges between D53 and K30 and D54 and R28 at the contact region of one pilin and four neighbouring pilins. C. Helical distribution of salt bridges along the GS pilus fiber. D. Salt bridges in the Asp2 pilus, which carries alanine replacements in D53 and D54, involve E48, E60, and S61 and strengthen hydrophobic interactions in the pilus fiber core.

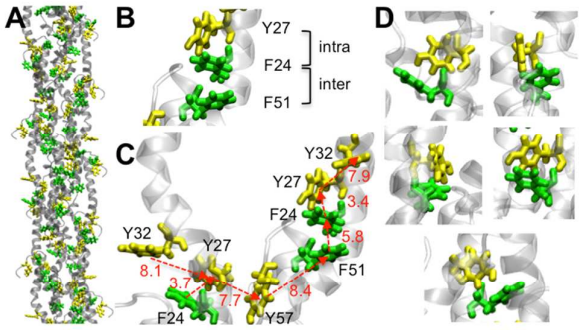

FIGURE 3. Clustering of aromatic residues in the GS pilus fiber. A. Snapshot of an average pilus structure resulting from the MD simulations showing the uniform distribution of aromatics (tyrosines, yellow; phenyalanines, green). B. Intra- and inter-molecular dimers (F24-Y27 and F51-F24, respectively) at the pilin-pilin contact region. C. Inter-aromatic distances in putative axial and transversal paths of the GS pilus. D. Typical geometric configurations (parallel-displaced and T-shaped) of the intramolecular F24-Y27 dimers.

neighboring pilins in the pilus fiber.[6] The conserved pilin rise also promoted electrostatic contacts between charged residues of one pilin and those of four neighboring pilins. The salt bridges were always between D53 and K30 and D54 and R28 (Figure 2B), with inter-chain distances fluctuating between 10 and 12 Å during the dynamic simulations. Furthermore, the salt bridges were arranged as a right-sided helix along the pilus fiber, following the helical assembly of the pilins (Figure 2C).

The inter-chain distance between D53 and D54 (10-12 Å) and the positively charged residues of the salt bridges maintained the pilins' α1-C domains slightly bent away from the axis of the fiber core (Figure 2B). Such conformational rearrangement exposed hydrophobic residues of the α-helices to the solvent during the simulations (Figure 1E). Consistent with this, replacing D53 and D54 with alanines (Asp2 pilus) promoted hydrophobic interactions along the full length of the helices (Figure 2D). Furthermore, new salt bridges formed between the positively charged amino acids (R28 and K30) and E48, E60 and S61 (Figure 2D). As a result, the C-t random coils, where E60 and S61 are located, were brought closer to the pilus fiber core and lost their structural plasticity.

Distribution and geometry of the pilin's aromatic residues in the GS pilus

The conformation of the pilins in the assembly, which were maintained by hydrophobic interactions of the α1-N domains and electrostatic contacts, also clustered the aromatic residues of neighboring subunits along and across the pilus fiber (Figure 3A). The aromatic contacts were both intramolecular (e.g., F24-Y27) and intermolecular (e.g., F51-F24) (Figure 3B) and formed both longitudinal and transversal paths for electron transfer (Figure 3C). The longitudinal path is consistent with a protein fiber that functions as a nanowire. The transversal path, on the other hand, could transfer electrons laterally to the most external of the aromatic residues, Y57, which could then reduce external electron acceptors such as Fe(III) oxides [1] and uranium.[2]

Inter-aromatic distances in the longitudinal and transversal paths ranged from ~3.5 to 8.5 Å (Figure 3C). These distances are optimal for multistep hopping reactions.[40, 41] Furthermore, a subset of aromatic dimers are close enough (~ 3.5 Å) to allow for π stacking and metallic conductance.[42] However, the geometric configuration of the dimers was typically of the parallel-displaced or T-shaped type, rather than the sandwich configuration that is necessary for π stacking. The intramolecular F24-Y27 contacts, for example, positioned the aromatic rings closer to each other (~ 3.5 Å) than any other dimer, but the geometry of the contacts during the simulations was always of the parallel-displaced or T-shaped type (Figure 3D).

Co-localization of aromatic and charged amino acids in the GS pilus fiber

All of the aromatic residues were in close proximity to charged residues. A transversal view of the GS pilus helps visualize the uniform distribution of aromatics across the fiber and the

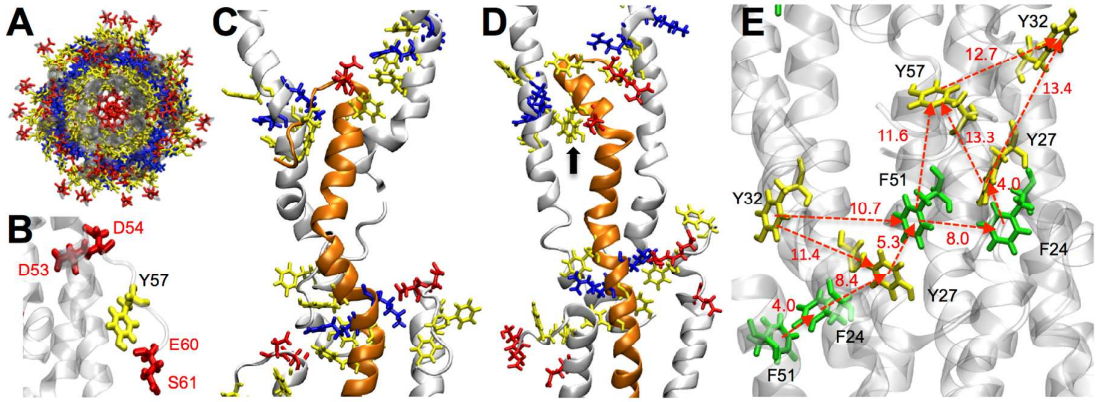

FIGURE 4. Spatial distribution of aromatics and charged residues. A-C. Top view (A) and details of the C-t random coil (B) or pilus fiber core (C) of the WT GS pilus showing the distribution of aromatics (yellow) and charged amino acids (acidic, red; basic, blue). D-E. Configuration (D) and inter-aromatic distances (E) of aromatics in the Asp2 pilus, which carries alanine replacements in D53 and D54. Arrow in (D) points at an intermolecular Y27-F51 dimer with aromatic rings stacked in a sandwich configuration. Phenylalanines in (E) are shown in green to distinguish them from the tyrosines (yellow).

preferential localization of charged residues in the fiber's core (positive charges) or pilus surface (negative charges) (Figure 4A). The positively-charged amino acids are buried in the pilus fiber core, whereas the negatively-charged amino acids predominantly reside in the areas of the pilus with highest exposure to the solvent such as the upper region of the α1 domain and the C-t random coil. Three of the negatively-charged residues (D53, D54, and E60) were in close proximity to Y57, the terminal tyrosine of the transversal charge transport path (Figure 4B). Also in this region is the last residue of the pilin, S61, which contributes with negative charges from its hydroxyl side chain and the free carboxyl group of the amino acid backbone. The concentration of negative charges in this exposed region of the GS pilus is expected to facilitate interactions with positively charged electron acceptors such as Fe(III) oxides and the uranyl cation. This is also the region of the pilin that fluctuates the most in the MD simulations, which is predicted to promote the binding of extracellular electron acceptors as well.

As we described earlier, D53 and D54 form salt bridges with positively-charged residues (K30 and R28, respectively) of the mid-region of neighboring pilins, where most of the aromatics cluster (Figure 4C). Electrostatic interactions in this region could affect the configuration of the aromatic residues and their reduction potential, thus influencing the rates of electron transfer. Consistent with this prediction, alanine replacements in D53 and D54 (Asp2 pilus) also rearranged the aromatic contacts (Figure 4D). Some of the intermolecular phenylalanine (F51-F24) dimers were, for example, replaced by intermolecular F51-Y27 contacts (Figure 4E). The new intermolecular contacts are typically in parallel-displaced configurations, but sandwich configurations between F51-Y27 were also observed in some regions of the pilus fiber core during the simulations (Figure 4D, arrow). Also notable is the rearrangement of the side chains of tyrosines Y27 and Y32 in the Asp2 pilus, which are now oriented to opposite sides of the α-helix and no longer form intramolecular contacts (Figure 4E). Furthermore, the range of inter-aromatic distances in the Asp2 pilus (~4 to 13 Å) increased (Figure 4E) compared that of the WT pilus (3.5-8.5 Å). The largest distance increases in the Asp2 pilus were for aromatics of the transversal pathway (Figure 4E). In the WT pilus, for example, transversal paths to Y57 were possible from Y27 and F51, which were at ~ 8 Å distances (Figure 3C). In the Asp2 pilus, the closest aromatic side chains to Y57 are F51, Y32, and Y27, which are located 11.6, 12.7, and 13.3 Å apart, respectively. Such distances can still support multistep hopping but the rates of electron transfer are expected to decrease.

Spatial distribution of aromatics and electrostatic potentials in the pilus fiber

The spatial distribution of aromatics and charged residues was also investigated by comparing the aromatic density and electrostatic potential maps of the WT pilus (Figure 5A and B, respectively). The aromatic isodensity map shows the average position of the aromatic residues over the 70 ns MD trajectories and highlights the uniform distribution of aromatics along the pilus and the helical path they create for charge transport during the simulations (Figure 5A). This contrasts with the reduced and non-helical distribution of aromatic density in a Tyr3 pilus fiber, which no longer has the three tyrosines (Y27, Y32, and Y57) of the pilin (Figure 5A).

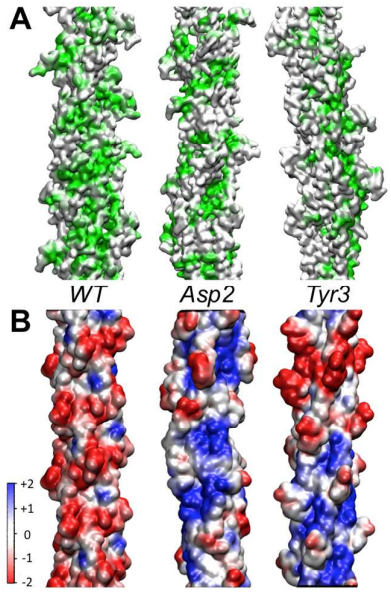

FIGURE 5. Aromatic (green) isodensity (A) and electrostatic (blue, positive; red, negative) potential (B) maps of the WT, Asp2, and Tyr3 pili. Color bar in (B), Volts.

The helical distribution of the aromatic-dense regions in the WT pilus matched well the helical arrangement of the regions of negative potential, which also formed a right-handed helix along the pilus fiber (Figure 5B). Negatively-charged residues (D53, D54, E60, and the terminal S61 residue) in the pilins' C-t regions contributed greatly to the surface negative potentials. As described earlier, two of the acidic residues (D53 and D54) form salt bridges with positively-charged amino acids (K30 and R28, respectively) of the mid-region of neighboring pilins (Figure 2C). The bridges bent the mid-region of the pilins away from the axis of the fiber core and aligned aromatics to form paths for axial and transversal charge transport (Figure 4). As a result, the helical region of negative potential was interspersed with the regions of highest aromatic density. This proximity also positioned D53 and D54 close to the tyrosines of the pilus fiber's core (Y27 and Y32), which could influence the mechanism and rates of electron transfer. By contrast, the areas of positive potential in the WT pilus were small and confined within the uncharged regions, thus minimizing charge trapping. In all of the simulations, the basic residues that contributed to the positive potential were R28 and K30, which are located in the pilin's mid-region in close proximity to Y27 and Y32 (Figure 4C). This arrangement keeps the aromatic orbitals empty and available to receive an electron, thus promoting electron hopping through the fiber's core.[43]

The helical distribution of aromatic density was still present in the Asp2 pilus (Figure 5A), consistent with the clustering of aromatics in the pilin assembly and formation of intermolecular and intramolecular contacts. However, the Asp2 mutation reduced the thickness of the aromatic-dense helical path along the pilus, indicating that on average the position of the aromatic residues during the MD simulations did not fluctuate as much as in the WT. This is expected for a more rigid pilus fiber, which no longer has the salt bridges that keep the pilins bent in the flexible mid-region (Figure 2D). The Asp2 mutation also reduced the regions of electronegative potential and disrupted their helical distribution (Figure 5B). Furthermore, it enlarged the areas of positive potential around tyrosine Y27, which could more easily trap electrons and reduce the overall rates of electron transfer. Furthermore, the overall charge of the pilus increased from -36 *e* (WT pilus) to 0 *e* in the Asp2 pilus. By contrast, the Tyr3 mutation did not affect the pilus net charge (-36 *e*) but did affect the spatial distribution of electrostatic potentials on the pilus surface (Figure 5B). The removal of the tyrosines' O-H molecular dipoles in the Tyr3 pilus thus disrupted the balanced charged distribution observed on the surface of the WT pilus and lead to a steep dipolar potential landscape (Figure 5B). As the pilus fiber is a periodic system, the dipolar landscape is expected to repeat itself along the pilus, creating alternating regions of negative and positive potential. Such periodic dipolar distribution creates large areas that can serve as electron traps (positive potentials) confined within high-energy barriers to the transport of electrons (negative potentials). Hence, electrons are predicted to sink at the "traps" of positive potential in the Tyr3 pilus fiber, unable to hop to the neighboring regions of negative potential.

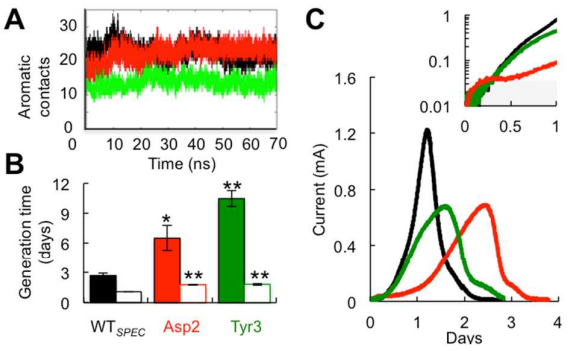

FIGURE 6. Role of aromatics and electrostatic contacts in charge transport studied in the WT (black), Asp2 (red), and Tyr3 (green) mutants. A. Number of aromatic contacts predicted in the MD simulations. B-C. In vivo effect of the Asp2 and Tyr3 mutations on the reduction of Fe(III) oxides in the absence (solid bars) or presence (clear bars) of the metal chelator NTA (B) and on the electrochemical activity of anode biofilms in MECs (C) in reference to the wild-type control strain WT_{SPEC}. Inset in C: semi logarithmic plot showing current production (Y axis, mA) during the first day of MEC operation (X axis, days); the phase of cell attachment (shaded area) precedes the exponential phase of current generation and biofilm growth.

Testing the model predictions in vivo

The Tyr3 mutation is predicted to severely affect pili functioning as an electronic conduit in vivo. Not only does the mutation disrupt the balanced distribution of charges (Figure 5B), it also removes the intramolecular Y27-Y32 dimers and reduces the number of aromatic contacts of the pilus fiber in half (Figure 6A). The mutation also replaces the most exposed aromatic residue (Y57), which we predicted to mediate the final step in electron transfer between the pili and external electron acceptors such as Fe(III) oxides. Supporting the model's predictions, introducing the Tyr3 mutation in *G. sulfurreducens* produced a mutant strain with severe growth defects during the reduction of Fe(III) oxides (Figure 6B). Generation times for the Tyr3 mutant strain were, for example, four-fold greater than the control WT_{SPEC} strain. However, the defect was chemically complemented in Fe(III) oxide cultures supplemented with the metal chelator NTA, which solubilizes Fe(III) from the Fe(III) oxides. The chelating activity of NTA therefore provides a soluble, chelated form of the ferric ion as an electron acceptor and alleviates the need of the cells to establish electronic contact with the Fe(III) oxides using the conductive pili.[1]

The growth and electrochemical activity of Tyr3 biofilms growing on anode electrodes poised at a metabolically oxidizing potential was also impaired (Figure 6C). The rates of current increase (mA/day) during the linear phase of current production, which correlate well with the exponential growth of the biofilm cells on the anode,[44] were three-times lower in the Tyr3 MECs (0.70 ± 0.08 mA/day, average and standard deviation of triplicate MECs) than in the control MECs driven by the WT_{SPEC} strain (2.11 ± 0.39 mA/day). Such differences cannot be attributed to defects in initial attachment to the electrode because the cell attachment efficiency, which can inferred from the lag phase that precedes the linear phase of current production,[34] was similar in the WT_{SPEC} and Tyr3 strains (Figure 6D, inset). Hence, as observed in the Fe(III) oxide cultures (Figure 6B), the Tyr3 mutation also reduced the respiratory rates of cells growing with an anode electrode as terminal electron acceptor. Furthermore, current maxima (0.63 ± 0.06 mA) by the Tyr3 anode biofilms were approximately half of the WT_{SPEC} biofilms (1.29 ± 0.4 mA) although both biofilms had reached a similar (~ 10 µm) thickness. This suggests that the catalytic current produced per cell in the Tyr3 biofilms is also reduced.

The model also predicts defects in the ability of the Asp2 pili to transfer electrons from the cell to extracellular electron acceptors such as Fe(III) oxides or electron carriers of the matrix of anode biofilms in MECs. This is because, although the number of aromatic contacts is the same as in the WT pilus (Figure 6A), the type, configuration, and distances of the aromatics in the contacts (Figure 4D and E) and the pilus surface properties (Figure 5B) are different. Consistent with the model's predictions, generation times during growth with Fe(III) oxides were two-fold greater in the Asp2 cultures compared to the WT_{SPEC} controls (Figure 6B). Furthermore, as we observed in the Tyr3 cultures, supplementing the Asp2

cultures with the metal chelator NTA to alleviate the need of the cells to transfer electrons via pili [1] chemically rescued the Asp2 mutant growth defect. The ability of the cells to discharge respiratory electrons in anode biofilms was also reduced as indicated by the four-fold decreases in the rates of current production (0.52 ± 0.11 mA/day) measured during the exponential phase of growth of the biofilm cells and the two-fold decreases in current maxima (0.68 ± 0.05 mA) (Figure 6C). Furthermore, the Asp2 cells initially colonized the electrode like the WT_{SPEC}, but they required more time (~12 h) to begin the exponential phase of biofilm growth and current generation (Figure 6D, inset). Hence, the *in vivo* studies support the model predictions that the local electrostatic environment around the aromatic contacts and the surface properties of the pilus influence the rates of electron transfer through the pili.

Discussion

The MD simulations produced a pilus structural model with features consistent with experimentally validated data. Hydrophobic contacts between neighboring α-helices were the major stabilizing forces of the pilus structure [6] and formed the central fiber core from which the flexible C-t random coil protruded at a 40° angle (Figure 1). The diameter of the fiber core in the favored conformer in solution was 35 Å, but was 47 Å when taking into account the volume of the C-t random-coiled segment. Such diameters are within the ranges estimated by atomic force microscopy (2-5 nm)[1, 11] and scanning tunneling microscopy.[11] Furthermore, the pilin rise in the assembly also fell within the ranges (~10.5 Å) reported for other bacterial pili.[6]

The conserved periodic rise of pilins in the assembly aligned residues F1 and E5 of neighboring pilins (Figure 2A), which are amino acids that interact *in vivo* to align the pilins during their assembly.[9] Also aligned were residues of opposite charges (D53 with K30 and D54 with R28), which formed salt bridges predicted to strengthen pilin-pilin contacts.[6] The salt bridges in the GS pilus maintained the bend in the pilin's mid-region, where a proline residue (P22) increases the flexibility of the peptide.[3] As a result, intermolecular gaps formed during the simulations in the regions where the salt bridges were located, exposing otherwise buried amino acids of the pilus core to the solvent (Figure 1E). Similar conformational rearrangements have been observed during steered MD simulations of the gonococcal GC pilus, which, as in the GS pilus, also make the interior of the pilus filament accessible to the solvent.[38] Such structural plasticity confers on the pilus fiber the mechanical properties and tensile strength that are key for its functions.[39]

The conformational arrangement of the pilins in the assembly clustered the aromatic residues (Figure 3) and created helical regions of high aromatic density that covered a continuous region of space along the pilus fiber during the MD simulations (Figure 5). The interatomic distances between aromatic residues in the GS pilus were approximately between 3.5 and 8.5 Å (Figure 3). Some inter-aromatic distances in this region are close enough to allow for π orbital stacking.[42] However, the aromatics did not form all the contacts at the same time, like a wire. Furthermore, the geometric configuration of all of the aromatic contacts were typically of the parallel-displaced or T-shaped, which are the prevalent configurations in proteins due to their superior stability.[45] The closest inter-aromatic distances corresponded, for example, to intramolecular dimers of F24 and Y27 (~3.5 Å) and intermolecular phenylalanine dimers between F51 and F24 residues of neighboring subunits (~6 Å). All of these contacts had parallel-displaced or T-shaped conformations during the simulations, rather than the sandwich configuration that could allow for π orbital stacking and metallic conductance. Moreover, the contacts involved aromatic residues (F24, Y27, and Y32) of the pilin's mid-helix, where resonance is greatest and charge hopping is predicted to be promoted.[8] As with other biological molecules,[46] the possibility exists that molecular motions occur *in vivo* that enable the formation of transient contacts in the more unstable sandwich dimer configuration and localized metallic regimes. However, metallic conduction requires the perfect alignment of all of the aromatic rings and without considerable displacement, as even small fluctuations can dramatically decrease the tunneling rates.[46] Hence, whereas some metallic regimes may transiently operate in the GS pilus *in vivo*, the prevailing mechanism of conduction supported by the MD simulations is that of multistep hopping.

Long-range charge hopping through the GS pilus is possible if amino acids with oxidizable side chains such as tyrosines are clustered sufficiently in the assembly so as to maintain side chain distances (sometimes of more than 20 Å) that permit successive short and fast electron transfer steps.[47] Consistent with their predicted role in electron transfer, replacing the pilin's three tyrosines with alanines (Tyr3 mutation) reduced the number of aromatic contacts of the pilus fiber in half and impaired the ability of the Tyr3 cells to reduce Fe(III) oxides unless in the presence of the metal chelator NTA (Figure 6), which alleviates the need for the cells to use pili to establish electronic contact with the insoluble electron acceptor.[1] In addition, the Tyr3 mutation reduced the rates of current increase during the linear phase of current production (Figure 6). This phase correlates well with the exponential growth of the biofilm cells on the anode electrode.[44] Hence, the reduced rates of current increase observed in the Tyr3-driven MECs are consistent with a mutant unable to efficiently discharge respiratory electrons to the biofilm matrix.

The clustering of aromatic side chains in the pilus created paths for transversal charge transport to a terminal tyrosine (Y57) (Figure 3). Y57 is located on the pilin's C-t random coil, the most exposed region of the pilin in the fiber. This is also a flexible domain, whose angle with respect to the helix region fluctuates in solution, a dynamic feature that could promote the binding of extracellular electron acceptors. In addition, Y57 is positioned on the pilus surface in close proximity to the carboxyl side chains of the three negatively-charged amino acids (D53, D54, and E60) and the carboxyl group of the terminal serine residue of the pilin (S61). Together, these

residues cage Y57 in a region of negative electrostatic potential and could promote the binding of cationic ligands in the insoluble Fe(III) oxides and the soluble uranyl cation. Upon binding, the carboxyl ligands also position the electron acceptors close to the terminal Y57 relay amino acid, thus facilitating the last step in electron transfer. Experimental evidence exists in support of this model: the atomic environment of the pili-bound uranium modeled from the uranium L_{III}-edge Extended X-ray Absorption Spectroscopy (EXAFS) spectra is that of a reduced U(IV) atom coordinated by two bidentate carbon ligands such as the carboxyl coordinations involving amino acids.[2]

The inter-aromatic distances and configuration of the aromatic residues involved in the contacts also depended on the local electrostatic environment. We observed, for example, that the Asp2 mutation did not affect the average number of aromatic contacts (Figure 6A) because, in the absence of salt bridges involving D53 and D54, new salt bridges formed that brought the helices closer together, thus promoting tight pilin-pilin contacts via hydrophobic interactions and the clustering of aromatics (Figure 2D). However, the areas of the pilus of highest aromatic density no longer co-localized with the regions of negative potential and were, instead, confined within large regions of positive potential where electrons could be easily trapped (Figure 5A). Furthermore, the configuration of the aromatic residues changed and, with it, the type of aromatics involved in the contacts and inter-aromatic distances (Figure 4D and E). The two negatively charged residues replaced with alanines in the Asp2 pilus (D53 and D54) are in close proximity to most of the pilin's aromatic residues (Figure 4) and are predicted to influence the local electrostatic interactions and the configuration of aromatic contacts required for optimal rates of electron transfer.[48] Furthermore, the close proximity of the pilin's three tyrosines and D53 and D54 could allow the aspartic residues to receive a proton from them, thereby reducing the oxidation potential of the tyrosines to the low levels that operate in biological systems.[49] This mechanism of proton-coupled electron transfer results in the transient protonation of acidic residues and tunes the oxidation potential of the neighboring aromatic residues to enable fast rates of electron transfer.[50] Not surprisingly, the Asp2 mutant reduced Fe(III) oxides at rates slower than the WT_{SPEC} control strain though the defect was not as severe as the Tyr3, which no longer has tyrosines in the aromatics pathways. In addition, the rates of current increase by the Asp2 cells in MECs were lower than the WT_{SPEC} but similar to the Tyr3 (Figure 6), consistent with mutations that reduced the ability of the pili to discharge respiratory electrons while growing on the anode electrode. Maximum current by fully-grown Asp2 biofilms was also reduced significantly (Figure 6), suggesting that the catalytic current generated per cell was lower. The electrochemical activity of the biofilms depends on the conductivity of the pili [51] as well as its ability to stabilize and support the multilayered biofilm community.[5] The stability of the biofilm matrix depends, in turn, on electrostatic interactions between the matrix components.[52, 53] Such interactions are likely to be significantly altered in the Asp2 biofilms due to the unique charge surface properties of the Asp2 pilus (Figure 5) and could explain the delays in current initiation (~12 h) observed after the cells had attached to the electrode (Figure 6). Furthermore, the net charge of the Asp2 pilus was increased (0 *e*, rather than the -36 *e* calculated for the WT and Tyr3 pilus fibers), which could also affect the ability of the pili to transfer electrons to redox-active components of the biofilm matrix such as *c*-cytochromes.

Conclusions

The theoretical and experimental results support a model of a GS pilus fiber evolved in structure and amino acid composition as a medium for charge transport. The packing, alignment, and geometric configuration of aromatic residues are consistent with a mechanism for charge transport dominated by multistep hopping. Furthermore, the local electrostatic environment around the aromatic contacts influenced the aromatic configuration to promote efficient electron transfer *in vivo*. Metallic regimes, if they occur *in vivo*, would be transient and induced by the flexible and dynamic structure of the pilus fiber in solution. Complex electronic behaviors are not unusual in nanowires, due to the confinement of electrons in the radial direction resulting from the high length-to-diameter ratio, which makes charge transport particularly sensitive to structural perturbations. Single-walled carbon nanotubes, for example, display metallic or semiconducting conduction as a function of their diameter and chirality.[54] Such complex electronic behaviors may be enhanced in the GS pili *in vivo* due to the dynamic nature of the appendages and may help modulate the rates of charge transport to the respiratory needs of the cell.

Acknowledgements

We thank Mauricio Domingues Coutinho-Neto for helpful discussions about the MD modeling experiments and Allison P. Speers for assistance with the Fe(III) oxide cultures. The authors also acknowledge the resources and technical support provided by the High Performance Computing Center (HPCC) at Michigan State University. This work was supported by a grant (MCB-1021948) from the National Foundation to GR and funds from The São Paulo Research Foundation (FAPESP) and the Brazilian National Council for Scientific and Technological Development (CNPq) to GTF.

References

1. G. Reguera, K. D. McCarthy, T. Mehta, J. S. Nicoll, M. T. Tuominen and D. R. Lovley, *Nature*, 2005, 435, 1098-1101.
2. D. L. Cologgi, S. Lampa-Pastirk, A. M. Speers, S. D. Kelly and G. Reguera, *Proc. Natl. Acad. Sci. USA*, 2011, 108, 15248-15252.
3. P. N. Reardon and K. T. Mueller, *J. Biol. Chem.*, 2013, 288, 29260-29266.

4. G. Reguera, K. P. Nevin, J. S. Nicoll, S. F. Covalla, T. L. Woodard and D. R. Lovley, *Appl. Environ. Microbiol.*, 2006, 72, 7345-7348.
5. G. Reguera, R. B. Pollina, J. S. Nicoll and D. R. Lovley, *J. Bacteriol.*, 2007, 189, 2125-2127.
6. L. Craig, N. Volkmann, A. S. Arvai, M. E. Pique, M. Yeager, E. H. Egelman and J. A. Tainer, *Mol. Cell*, 2006, 23, 651-662.
7. V. Pelicic, *Mol. Microbiol.*, 2008, 68, 827-837.
8. G. T. Feliciano, A. J. R. da Silva, G. Reguera and E. Artacho, *J. Phys. Chem. A*, 2012, 116, 8023-8030.
9. L. Craig and J. Li, *Curr. Opin. Struct. Biol.*, 2008, 18, 267-277.
10. Y.-g. K. Shin, M. D. Newton and S. S. Isied, *J. Am. Chem. Soc.*, 2003, 125, 3722-3732.
11. J. P. Veazey, G. Reguera and S. H. Tessmer, *Phys. Rev. E*, 2011, 84, 060901.
12. N. S. Malvankar, S. E. Yalcin, M. T. Tuominen and D. R. Lovley, *Nature nanotechnology*, 2014, DOI: 10.1038/nnano.2014.236.
13. N. S. Malvankar, M. Vargas, K. P. Nevin, A. E. Franks, C. Leang, B. C. Kim, K. Inoue, T. Mester, S. F. Covalla, J. P. Johnson, V. M. Rotello, M. T. Tuominen and D. R. Lovley, *Nature nanotechnology*, 2011, 6, 573-579.
14. P. S. Bonanni, D. Massazza and J. P. Busalmen, *Phys. Chem. Chem. Phys.*, 2013, 15, 10300-10306.
15. N. S. Malvankar, M. Vargas, K. Nevin, P. L. Tremblay, K. Evans-Lutterodt, D. Nykypanchuk, E. Martz, M. T. Tuominen and D. R. Lovley, *MBio*, 2015, 6, e00084.
16. H. Yan, C. Chuang, A. Zhugayevych, S. Tretiak, F. W. Dahlquist and G. C. Bazan, *Adv. Mater.*, 2015, 27, 1908-1911.
17. L. Craig, M. E. Pique and J. A. Tainer, *Nat. Rev. Microbiol.*, 2004, 2, 363-378.
18. G. Launay and T. Simonson, *BMC Bioinformatics*, 2008, 9, 427.
19. P. Aloy, H. Ceulemans, A. Stark and R. B. Russell, *J. Mol. Biol.*, 2003, 332, 989-998.
20. A. Nurisso, A. Daina and R. C. Walker, *Methods Mol. Biol.*, 2012, 857, 137-173.
21. B. Hess, C. Kutzner, D. van der Spoel and E. Lindahl, *J. Chem. Theory Comput.*, 2008, 4, 435-447.
22. C. Kutzner, D. van der Spoel, M. Fechner, E. Lindahl, U. W. Schmitt, B. L. de Groot and H. Grubmuller, *J. Comput. Chem.*, 2007, 28, 2075-2084.
23. D. Van Der Spoel, E. Lindahl, B. Hess, G. Groenhof, A. E. Mark and H. J. Berendsen, *J. Comput. Chem.*, 2005, 26, 1701-1718.
24. K. Arnold, L. Bordoli, J. Kopp and T. Schwede, *Bioinformatics*, 2006, 22, 195-201.
25. L. Bordoli, F. Kiefer, K. Arnold, P. Benkert, J. Battey and T. Schwede, *Nat. Protocols*, 2008, 4, 1-13.
26. V. Hornak, R. Abel, A. Okur, B. Strockbine, A. Roitberg and C. Simmerling, *Proteins: Structure, Function, and Bioinformatics*, 2006, 65, 712-725.
27. W. L. Jorgensen, J. Chandrasekhar, J. D. Madura, R. W. Impey and M. L. Klein, *J. Chem. Phys.*, 1983, 79, 926.
28. B. Hess, H. Bekker, H. J. C. Berendsen and J. G. E. M. Fraaije, *J. Comput. Chem.*, 1997, 18, 1463-1472.
29. W. Humphrey, A. Dalke and K. Schulten, *J. Mol. Graph.*, 1996, 14, 33-38, 27-38.
30. W. L. Jorgensen and J. Tirado-Rives, *J. Am. Chem. Soc.*, 1988, 110, 1657.
31. S. Pronk, S. Pall, R. Schulz, P. Larsson, P. Bjelkmar, R. Apostolov, M. R. Shirts, J. C. Smith, P. M. Kasson, D. van der Spoel, B. Hess and E. Lindahl, *Bioinformatics*, 2013, 29, 845-854.
32. F. Caccavo, Jr., D. J. Lonergan, D. R. Lovley, M. Davis, J. F. Stolz and M. J. McInerney, *Appl. Environ. Microbiol.*, 1994, 60, 3752-3759.
33. M. V. Coppi, C. Leang, S. J. Sandler and D. R. Lovley, *Appl. Environ. Microbiol.*, 2001, 67, 3180-3187.
34. A. M. Speers and G. Reguera, *Appl. Environ. Microbiol.*, 2012, 78, 437-444.
35. B. C. Kim, C. Leang, Y. H. Ding, R. H. Glaven, M. V. Coppi and D. R. Lovley, *J. Bacteriol.*, 2005, 187, 4505-4513.
36. L. L. Stookey, *Anal. Chem.*, 1970, 42, 779-781.
37. J. B. McKinlay, J. G. Zeikus and C. Vieille, *Appl. Environ. Microbiol.*, 2005, 71, 6651-6656.
38. J. L. Baker, N. Biais and F. Tama, *PLoS Comput. Biol.*, 2013, 9, e1003032.
39. N. Biais, D. L. Higashi, J. Brujić, M. So and M. P. Sheetz, *Proc. Natl. Acad. Sc.i USA*, 2010, 107, 11358-11363.
40. M. Cordes, A. Kottgen, C. Jasper, O. Jacques, H. Boudebous and B. Giese, *Angew. Chem. Int. Ed. Engl.*, 2008, 47, 3461-3463.
41. C. Shih, A. K. Museth, M. Abrahamsson, A. M. Blanco-Rodriguez, A. J. Di Bilio, J. Sudhamsu, B. R. Crane, K. L. Ronayne, M. Towrie, A. Vlcek, Jr., J. H. Richards, J. R. Winkler and H. B. Gray, *Science*, 2008, 320, 1760-1762.
42. N. Ashkenasy, W. S. Horne and M. R. Ghadiri, *Small*, 2006, 2, 99-102.
43. C. Wittekindt, M. Schwarz, T. Friedrich and T. Koslowski, *J. Am. Chem. Soc.*, 2009, 131, 8134-8140.
44. E. Marsili, J. Sun and D. R. Bond, *Electroanalysis*, 2010, 22.
45. G. B. McGaughey, M. Gagné and A. K. Rappé, *J. Biol.l Chem.*, 1998, 273, 15458-15463.
46. J. L. Bredas, J. P. Calbert, D. A. da Silva Filho and J. Cornil, *Proc. Natl. Acad. Sci. USA*, 2002, 99, 5804-5809.
47. B. Giese, M. Graber and M. Cordes, *Curr. Opin. Chem. Biol.*, 2008, 12, 755-759.
48. C. R. Martinez and B. L. Iverson, *Chem. Sci.*, 2012, 3, 2191-2201.
49. S. Y. Reece and D. G. Nocera, *Annu. Rev. Biochem.*, 2009, 78, 673-699.
50. J. Stubbe, D. G. Nocera, C. S. Yee and M. C. Chang, *Chem. Rev.*, 2003, 103, 2167-2201.
51. M. Vargas, N. S. Malvankar, P. L. Tremblay, C. Leang, J. A. Smith, P. Patel, O. Synoeyenbos-West, K. P. Nevin and D. R. Lovley, *MBio*, 2013, 4, e00105-00113.
52. X. Chen and P. S. Stewart, *Appl. Microbiol. Biotechnol.*, 2002, 59, 718-720.
53. H. C. Flemming and J. Wingender, *Nat. Rev. Microbiol.*, 2010, 8, 623-633.
54. T. Durkop, B. M. Kim and M. S. Fuhrer, *J. Phys.: Condens. Matter*, 2004, 16, R553-R580.